POLITECNICO DI TORINO
Repository ISTITUZIONALE

Simultaneous X-Ray Diffraction and Tomography Operando Investigation of Aluminum/Graphite Batteries

Original
Simultaneous X-Ray Diffraction and Tomography Operando Investigation of Aluminum/Graphite Batteries / Elia, G.A., Greco, G., Kamm, P.H., Garcia-Moreno, F., Raoux, S., Hahn, R.. - In: ADVANCED FUNCTIONAL MATERIALS. - ISSN 1616-301X. - ELETTRONICO. - 30:43(2020), p. 2003913. [10.1002/adfm.202003913]

Availability:
This version is available at: 11583/2959195 since: 2022-03-23T11:24:07Z

Publisher:
Wiley-VCH Verlag

Published
DOI:10.1002/adfm.202003913

Terms of use:

This article is made available under terms and conditions as specified in the corresponding bibliographic description in the repository

Publisher copyright

(Article begins on next page)

18 November 2026

ADVANCED FUNCTIONAL MATERIALS
www.afm-journal.de

Simultaneous X-Ray Diffraction and Tomography Operando Investigation of Aluminum/Graphite Batteries

Giuseppe Antonio Elia, Giorgia Greco,* Paul Hans Kamm, Francisco García-Moreno, Simone Raoux, and Robert Hahn*

Rechargeable graphite dual-ion batteries are extremely appealing for grid-level stationary storage of electricity, thanks to the low-cost and high-performance metrics, such as high-power density, energy efficiency, long cycling life, and good energy density. An in-depth understanding of the anion intercalation mechanism in graphite is fundamental for the design of highly efficient systems. In this work, a comparison is presented between pyrolytic (PG) and natural (NG) graphite as positive electrode materials in rechargeable aluminum batteries, employing an ionic liquid electrolyte. The two systems are characterized by operando synchrotron energy-dispersive X-ray diffraction and time-resolved computed tomography simultaneously, establishing a powerful characterization methodology, which can also be applied more in general to carbon-based energy-related materials. A more in-depth insight into the $AlCl_4^-$/graphite intercalation mechanism is obtained, evidencing a mixed-staged region in the initial phase and a two-staged region in the second phase. Moreover, strain analysis suggests a correlation between the irreversibility of the PG electrode and the increase of the inhomogenous strain. Finally, the imaging analysis reveals the influence of graphite morphology in the electrode volume expansion upon cycling.

1. Introduction

Aluminum batteries are considered sustainable candidates for the realization of electrochemical storage systems.[1,2] Aluminum combines lightweight with low cost and elevated abundance (the most abundant metal element in the Earth's crust).[1,3,4] The Al metal anode possesses the highest volumetric capacity among metals, 8.04 Ah cm^{-3}, four times higher than Li, and one order of magnitude higher than the graphite anodes used in conventional lithium-ion batteries, 0.84 Ah cm^{-3}.[1,5] Furthermore, the gravimetric capacity of 2.98 Ah g^{-1} of the Al metal anode system is excellent. However, for Al-systems, only batteries with a relatively low voltage can be realized, generally not higher than 2 V. Among the various electrochemical cells proposed so far, including metal sulfide,[6,7] metal oxide,[8–10] organic electrode,[11] and sulfur,[12–15] the highest performances in terms of cycle life and rate capability have been reported employing graphite positive electrodes.[16–18] However, aluminum/graphite cells are characterized by a limited energy density, due to limited delivered capacity, relatively low voltage, and the electrolyte consumption during the cell operation.[19–21] Nevertheless, the expected low cost of materials employed and the extremely high rate capability, being in the range of electrochemical supercapacitors make this system extremely appealing for grid-level stationary storage of electricity.[20,21] The reaction mechanism of the Al/graphite cell involves the anion ($AlCl_4^-$) intercalation between graphite layers.[22–25] The intercalation process follows a staging mechanism with the formation of graphite intercalated compounds (GICs).[26,27] The investigation and understanding of the reaction mechanisms can provide valuable information for the further development of the Al/graphite system. Moreover, anion intercalation processes are gaining increased attention in the battery community for application in Li, Na, K, Mg, Ca batteries, and hybrid systems.[28] The expected low cost and the high performance (power density ≈3–175 kW kg^{-1}, energy efficiency ≈80–90%, long cycling life, and good energy density up to 200 Wh kg^{-1}) make those systems extremely appealing.[21] A more comprehensive understanding of anion intercalation processes in graphite is fundamental for the further development of this kind of system. In the present work, we investigate in detail the intercalation mechanism of the $AlCl_4^-$ anion in graphite by operando energy-dispersive X-ray diffraction (ED-XRD) combined with simultaneous tomography. The obtained results give new insights

Dr. G. A. Elia[+]
Technische Universität Berlin
Research Center of Microperipheric Technologies
Gustav–Meyer-Allee 25, Berlin D-13355, Germany
E-mail: elia@kit.edu

Dr. G. Greco, Dr. P. H. Kamm, Dr. F. García-Moreno, Prof. S. Raoux
Helmholtz-Zentrum Berlin für Materialien und Energie GmbH
Hahn-Meitner-Platz 1, Berlin D-14109, Germany
E-mail: giorgia.greco@helmholtz-berlin.de

Prof. S. Raoux
Institut für Physik
Humboldt Universität Berlin
Newtonstrasse 15, Berlin D-12489, Germany

Dr. R. Hahn
Fraunhofer-Institut für Zuverlässigkeit und Mikrointegration
Gustav-Meyer-Allee 25, Berlin D-13355, Germany

The ORCID identification number(s) for the author(s) of this article can be found under https://doi.org/10.1002/adfm.202003913.

© 2020 The Authors. Published by Wiley-VCH GmbH. This is an open access article under the terms of the Creative Commons Attribution License, which permits use, distribution and reproduction in any medium, provided the original work is properly cited.

[+]Present address: Helmholtz Institute Ulm (HIU), Helmholtzstrasse 11, 89081 Ulm, Germany; Karlsruhe Institute of Technology (KIT), P.O. Box 3640, 76021 Karlsruhe, Germany

DOI: 10.1002/adfm.202003913

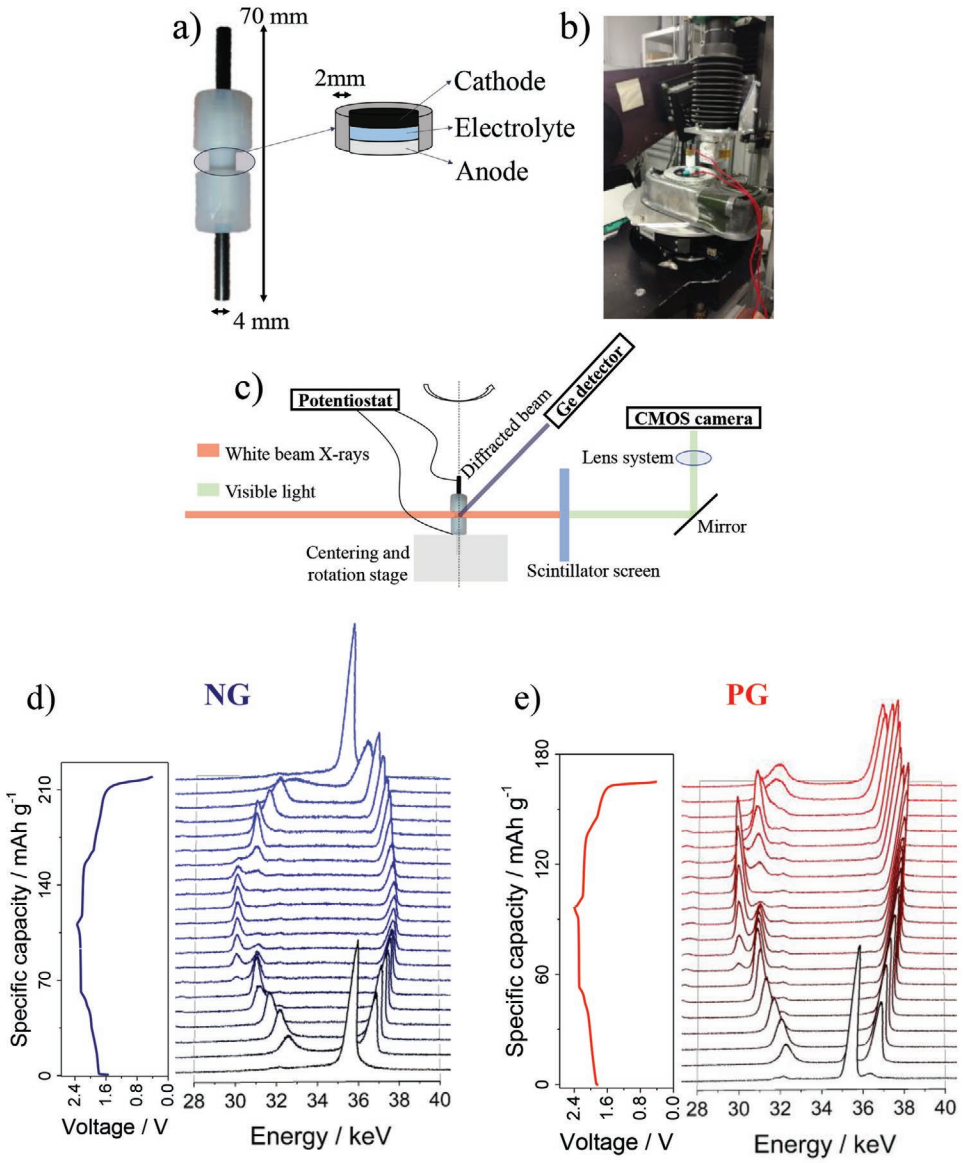

Figure 1. a) Schematic of the cell employed for the operando measurements. b) Photograph of the beamline apparatus employed to perform the operando diffraction and tomographic measurements. c) Schematic representation of the experimental set-up. Operando ED-XRD data of the d) NG electrode and e) of the PG electrode in the first cycle of the aluminum-graphite battery. The cycling test was performed at 25 mA g^{-1} current density and room temperature. The ED-XRD curves were displaced vertically for clarity. The voltage profile recorded during the test is reported along the ED-XRD spectra. The ED-XRD spectra are placed along the voltage plateau, corresponding to the cycling specific step.

into the intercalation mechanism, suggesting the influence of the inhomogenous strain in the reversibility of the process. Moreover, the imaging of the electrode upon operation reveals the severe volumetric change for both samples. These data are fundamental for the design of materials and cell configurations for future large-scale application of this battery system.

2. Results and Discussion

2.1. Operando XRD

Figure 1a reports the picture of the Swagelok type cell used for in operando electrochemical measurements. Figure 1b shows a photographic picture of the beamline setup, while a scheme of it is reported in Figure 1c.[29–31] Figure S1a in the Supporting Information compares the Al/NG cells voltage profiles obtained using our conventional[20,23,24,32] and the operando cell setup, showing a good overlap of the curves, thus indicating the validity of the employed configuration. Figure S1b in the Supporting Information demonstrates the long-term cycling performance of the Al/NG cell obtained using the operando cell setup, evidencing excellent stability for the 50 cycles of the test, i.e., for almost 10 days. The high energy of the beam can affect the investigated electrochemical system. Figure S2 in the Supporting Information shows the fifth cycle voltage profile of the NG cell during the operando measurement. The voltage drop

© 2020 The Authors. Published by Wiley-VCH GmbH

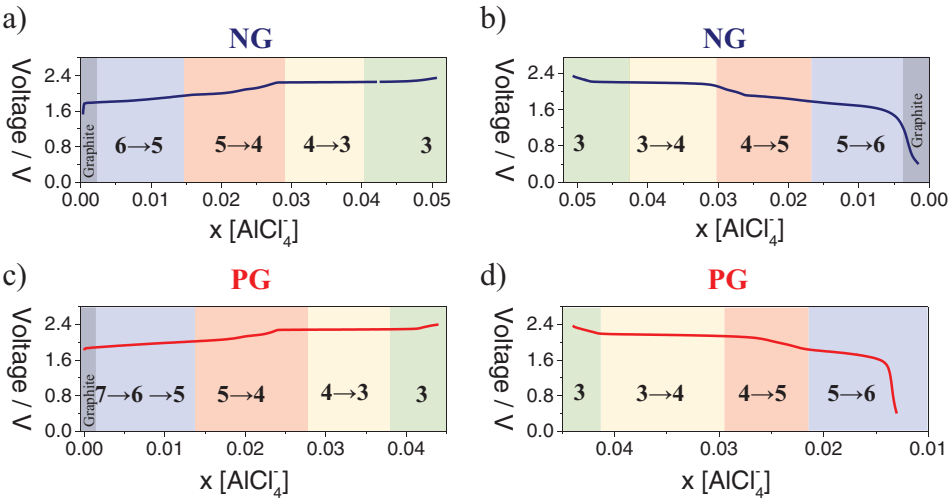

Figure 2. Evolution of the GIC staging during the first cycle for a,b) the Al/NG cell and c,d) the Al/PG cell. $x[AlCl_4^-]$ represents the mole of $AlCl_4^-$ anion intercalated for 1 mol of C.

corresponds to the period in which the cell is exposed to the beam. However, the voltage drop is almost negligible, being in the range of a few mV. The limited effect of the beam to the cell is most likely associated with the low absorbing power of the cell component (polytetrafluoroethylene (PTFE) and glassy carbon). On the contrary, for tests performed in coin cells, the effect is more substantial, due to the higher absorbing power of the stainless steel casing of the coin cell. In Figure S3 in the Supporting Information, the ED-XRD spectra of the pristine PG and NG materials are compared. The spectra were acquired from the cell at the open-circuit voltage (OCV) condition. The stacking of the graphite layers can be arranged in two configurations: ABA (2H) graphite and ABCA (3R) graphite structure. Both ED-XRD patterns show the (002) peak of the 2H graphite structure at an energy of ≈35 keV (*d*-spacing 0.335 nm), but also a minor contribution from the 3R graphite phase.[33] Additional peaks associated with the PTFE of the cell are identified. The presence of and ratio between the 2H and the 3R phases is not expected to influence the electrochemical behavior.[34]

Figure 1d,e report the operando ED-XRD of the graphite materials (NG electrode (Figure 1d) and the PG electrode (Figure 1e)) during the first (dis)charge cycle in the 28–40 keV energy range. The spectra obtained by measuring the Al/NG cell (Figure 1d) reveal that upon charging the (002) peak characteristic of graphite (at 35.5 keV) disappears with the formation of new peaks, indicating the formation of a GIC.[22–27] The overall electrochemical process is characterized by good reversibility, as shown in Figure S4a in the Supporting Information. The GIC formation upon charging is entirely reversed during discharging, as demonstrated by the reappearing of the initial (002) peak. On the contrary, the spectra obtained measuring the Al/PG cell (Figure 1e) show that for this system, the electrochemical process is not fully reversible. In fact, after full discharge, a stage-6 GIC is retained (Figure S4b, Supporting Information). However, analyzing the first charge process of NG and PG electrodes comparing Figure S4a and Figure S4b in the Supporting Information, we can recognize that both follow a very similar reaction path. Following the first cycle, the PG cell shows a very stable cycling behavior with a steady-state efficiency of about 98%, similar to the one obtained for the Al/NG cell (Figure S5, Supporting Information).[35] Moreover, the difference in delivered capacity between the two materials cannot be related to the different electrode loading. Figure S6 in the Supporting Information shows a comparison of a multi-rate test performed on the PG electrode with different active material loading. The measurement clearly evidences that at low current all the electrodes deliver similar capacity. The difference in the electrode loading starts to play a role when the current rate is increased.

The formation of the GIC involves the intercalation of the $AlCl_4^-$ species following a multi-staging process typical for the anion intercalation in graphite.[22,25,36–42] The staging behavior of the GIC during the electrochemical process can be evaluated from the ratio between $d_{(00n+2)}/d_{(00n+1)}$ peaks.[23,24,29,38,39,43,44] Table S1 in the Supporting Information reports the $d_{(n+2)}/d_{(n+1)}$ ratio calculation of some selected spectra and the relative evaluated stage.

Figure 2 shows the GIC staging evolution as a function of the voltage profile for the two investigated systems. The comparison of the staging evolution during the charging process for the Al/NG cell (Figure 2a) and the Al/PG cell (Figure 2c) indicates the formation of stage 7/6 in the initial phase of the intercalation reaching a stage-4 gradually for a charge capacity of about 60 mAh g^{-1} (i.e., $C[AlCl_4]_{0.027}$).[20] This initial phase appears in a mixed-staged region,[45] with a sloping voltage variation and a gradual shifting of the GIC peak positions. After about 60 mAh g^{-1}, the process proceeds in a two-staged region with a flat voltage plateau,[45] characterized by spectra evolution showing the disappearance of the peak associated with the stage-4 GIC and the appearing of the peak associated with the stage-3 GIC. The evaluated staging evolution is in agreement with the one obtained by Pan et al.[25] for a similar system. However, Pan et al.[25] observed that lower staging and, consequently, higher capacity could be obtained only at low temperatures, where the electrolyte decomposition kinetic is limited. Our results indicate that low staging can also be

© 2020 The Authors. Published by Wiley-VCH GmbH

formed at room temperature. The higher capacity at room temperature can be probably related to an optimized cell configuration.[18–20,46] Moreover, the XRD data reported by Pan et al.[25] focus on the intercalation process (charge), the de-intercalation (discharge) is not analyzed.

Besides the slight difference in the first cycle charge capacity (NG 110 mAh g^{-1} vs PG 100 mAh g^{-1}), the charging process is relatively similar for the two systems. On the contrary, the de-intercalation (discharge) process is remarkably different. For the NG, the de-intercalation process is perfectly symmetrical to the charge (Figure 2d), following the two-staged region for the 3→4 stages and subsequently the mixed-staged region from the stage-4 to GIC to high staging (6–7) until the initial graphite structure is obtained upon complete de-intercalation. However, for the Al/PG cell, the de-intercalation process is not fully reversible, and a stage-6 GIC is obtained after the discharge process. The results are in agreement with our previous reports,[20,23,24] suggesting that the microstructural differences between the two materials influence the de-intercalation process. The volumetric variation upon intercalation leads to a decrease of the porosity of the PG electrode, in turn leading to partial retention of the anion.[20,23,24] The partial retention of the anion results in a lower delivered capacity of the PG (70 mAh g^{-1}) with respect to the NG (110 mAh g^{-1}) electrode.[20]

Figure 3a reports the operando diffraction result of the fifth and the sixth cycle of the Al/NG cell cycling test, revealing that the (002) peak reappears unchanged after each (dis-)charge process. On the contrary, the partial anion retention of the PG in the first cycle limits the electrochemical activity of the PG to only 70% of the maximum available capacity. The partial reversibility of the PG is visualized in Figure 3b, reporting the operando diffraction results of the fifth and the sixth cycle, showing that the PG never comes back to graphite, but the electrochemical process proceeds between low-staging GIC (3–4) and high-staging GIC (5–6). The peculiar electrochemical behavior of the Al/PG cell is also confirmed for longer-term cycles, as evidenced in Figure S7 in the Supporting Information, reporting the operando diffraction result of the 50th cycle. Operando ED-XRD results are in good agreement with the calculations reported by Kaghazchi and co-workers,[22] indicating the formation of stage 5–6 to be completed with the beginning of the formation of stage-4 at about 18 mAh g^{-1} capacity, the stage-4 to be completed at about 70 mAh g^{-1} and the stage-3 at 95 mAh g^{-1}. Kaghazchi and co-workers attributed the capacity exceeding 95 mAh g^{-1} to the formation in the shell of the graphite particles stage-2 or 1 GIC.[22] Our experimental data cannot confirm the latter hypothesis due to the detection limits of the used technique.

The graphite strain evolution upon cycling was analyzed from the ED-XRD spectra, to acquire a more in-depth insight into the reaction mechanism. The ED-XRD peak width analysis can give us information about the crystallite size and lattice strain.[47] Crystallite size is a measure of the size of coherently diffracting domains. Lattice strain is a measure of the distribution of lattice constants arising from crystal imperfections, such as lattice dislocations, grain boundaries, and coherency stresses.[48] Crystallite size and lattice strain affect the peak width and intensity and shift the 2θ, or in our case, the energy peak positions. The effect of strain, both uniform and non-uniform, on the diffracted X-rays is illustrated in Figure S8 in the Supporting Information. If a homogenous strain is applied to grains at the right angle, the spacing of reflecting planes becomes smaller, resulting in a peak shift to larger angles. An inhomogenous strain results in a nonuniform distribution of plane spacings, thus leading to a broadening of the diffracted peaks.[49]

Additionally, the crystallite dimension also influences the peak width. However, the peak width derived from crystallite size varies as $1/\cos\theta$, whereas strain varies as $\tan\theta$. This difference in behavior as a function of the reciprocal of the lattice

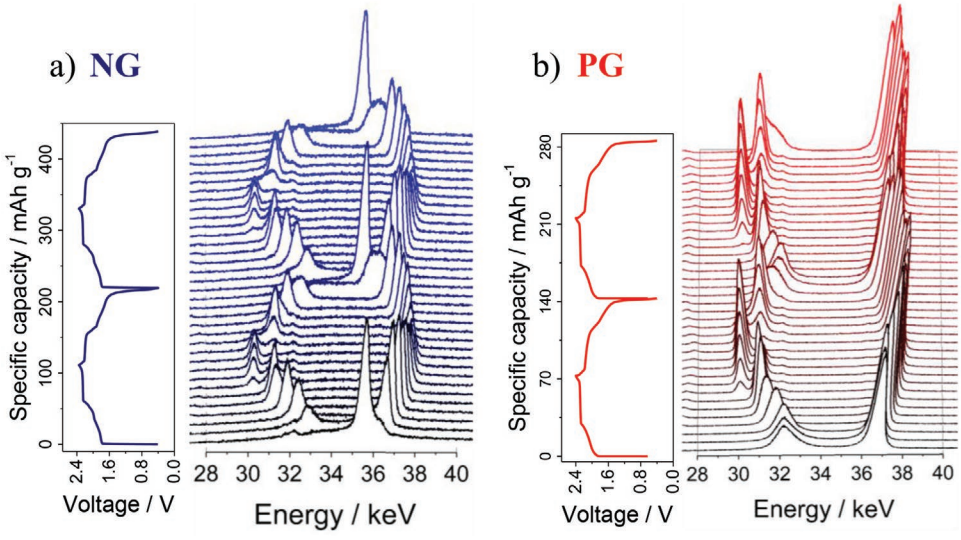

Figure 3. Battery charging behavior and operando ED-XRD spectra acquired at the synchrotron. Operando ED-XRD data of a) the NG and b) of the PG electrode of the fifth and sixth cycle of the aluminum-graphite battery. The cycling test was performed at 25 mA g^{-1} current and room temperature. The ED-XRD curves were displaced vertically for clarity. The voltage profile recorded during the test is reported along the ED-XRD spectra. The ED-XRD spectra are placed along the voltage plateau, corresponding to the cycling specific step.

© 2020 The Authors. Published by Wiley-VCH GmbH

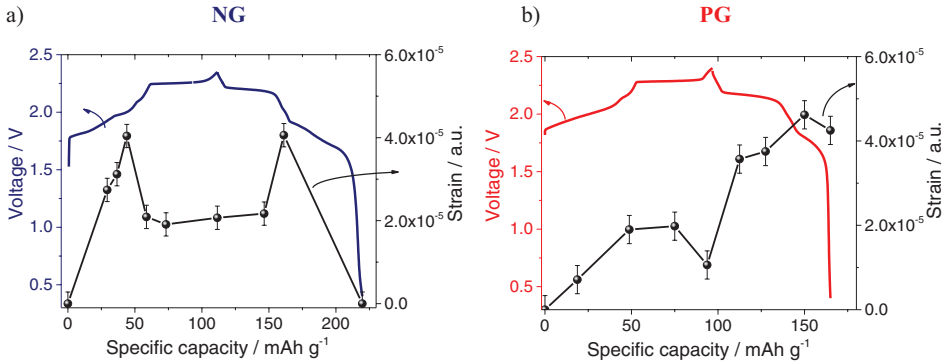

Figure 4. Evolution of the strain, calculated from operando ED-XRD data, as a function of the first cycle voltage profile for a) NG and b) PG. The cycling test was performed at 25 mA g^{-1} current and room temperature.

distance d^* enables one to discriminate between the size and strain effects on peak broadening. The Bragg peak width contribution from crystallite size is inversely proportional to the crystallite size.[50] Williamson–Hall (WH) analysis is a simplified integral breadth method where size-induced and strain-induced broadening are deconvoluted by considering the peak width as a function of d^*.[51] In ED diffraction, the relation between a lattice spacing $d(hkl)$ and the corresponding diffraction line $E(hkl)$ is easily derived from Bragg's equation.[29] **Figure 4** reports the correlation between the voltage profile and the evaluated strain for the first galvanostatic cycle of the Al/NG cell (Figure 4a) and the Al/PG cell (Figure 4b). The data obtained from the analysis are reported in Table S1 in the Supporting Information for the NG and in Table S2 in the Supporting Information for the PG electrode. Due to analysis approximations, the evaluation is focused on the trend and not on absolute values. The data obtained by the NG cell show an increase of the strain in the initial phase, up to 50 mAh g^{-1}, following a decrease and stabilization until the full charge. The discharge behavior is symmetrical to the charging process, with a stable value until 50 mAh g^{-1}, followed by an increase in the intermediate stage and a reduction of the value upon complete discharge. The trend indicates an increased strain in the initial phase of the intercalation (until stage-5). It is most likely associated with the low order in the intercalation mechanism, leading to an inhomogenous strain in the graphite. The strain value decreases in the stage-4 to stage-3 transition, in agreement with the more ordered intercalation processes. The results obtained with the PG electrode are quite different compared to the NG electrode (Figure 4b). For PG, the strain value increases upon charging, similar to the NG electrode. However, the strain decreases only in the last phase of the intercalation when a stage-3 GIC is reached. During the discharge process, a continuous increase of the strain values is observed from the beginning of the de-intercalation. The strain increase, in particular for the fully discharged state, reveals a very disordered and inhomogenous phase.

2.2. Operando X-Ray Tomography

The lattice expansion of the graphite upon $AlCl_4^-$ intercalation leads to a volumetric variation at the microscale of the graphite electrode.[24] The setup used in the present experiments allows following the structural evolution of the compound by ED-XRD and the electrode morphology evolution by the acquisition of tomographic images simultaneously. **Figure 5** reports the tomographic images obtained during the first cycle of the galvanostatic cycling test of the Al/NG cell (Figure 5a) and the Al/PG cell (Figure 5b). The figures show on the right side the voltage profile, and on the left the 3D reconstruction of the graphite electrodes. The circles on the voltage profile indicate the step of the cycling test at which the tomogram was acquired. The comparison of the NG and the PG evidences a different starting electrode morphology. The NG appears quite inhomogenous, with an average thickness of 47.9 ± 20.0 µm. The inhomogeneity reflects the nonoptimized electrode preparation.[20] Conventional electrode preparation is not possible for the NG because of highly corrosive electrolyte.[20] The PG electrode appears very homogenous, with a starting average thickness of 32.5 ± 3.1 µm.

Due to the limited spatial resolution of the images, it is not possible to evaluate in detail the morphological evolution of the electrode, such as the porosity.[24] The limited spatial resolution is related to the low X-ray absorption of graphite and the geometry of the imaging setup, as it is a compromise to allow both ED-XRD and tomography. However, the obtained data allowed us to follow the evolution of the electrode thickness upon cycling. The results of electrode thickness evolution during cycling are listed in Tables S3 and S4 in the Supporting Information for the NG and PG electrode, respectively. **Figure 6** reports the value of the electrode thickness as a function of the voltage profile for the Al/NG cell (Figure 6a) and the Al/PG cell (Figure 6b). The electrode thickness increases during the intercalation process for both materials. The PG shows a higher increase in the electrode thickness compared to the NG electrode. This behavior is associated with the peculiar morphology of the PG characterized by the preferential planar orientation of the graphite crystal.[24] Moreover, the different electrode preparation methods influence the thickness evolution during cycling. During the de-intercalation process, the electrode thickness decreases, however not returning to the initial state for the PG electrode. An elevated uncertainty characterizes the results obtained from the NG electrode. However, we observe symmetrical behavior for the (dis-)charge profile,

© 2020 The Authors. Published by Wiley-VCH GmbH

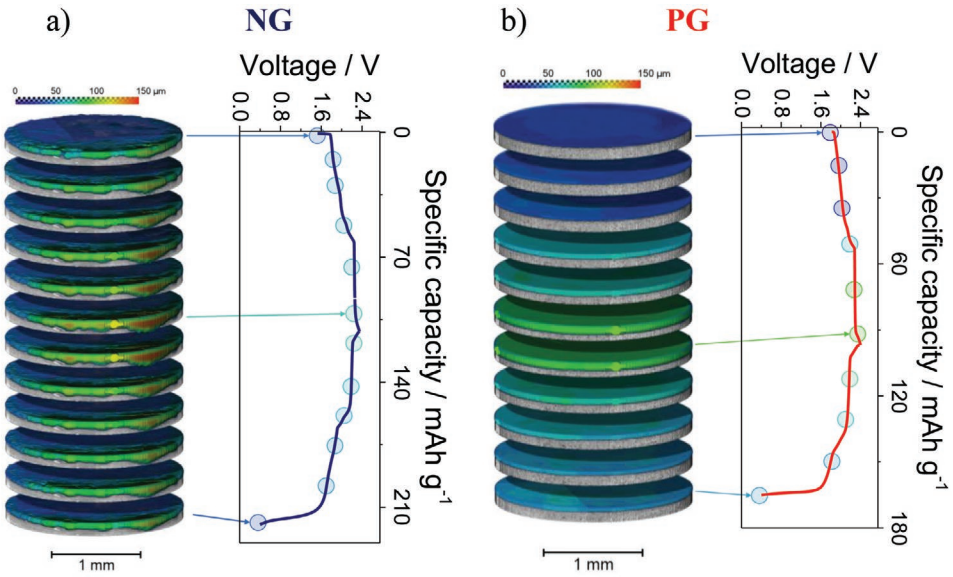

Figure 5. 3D tomographic images of the a) NG electrode and b) PG electrode upon cycling. The tomographic images were displaced vertically for clarity. The images are placed along the voltage plateau, corresponding to the cycling specific step. A circle underlines the moment of the cycling test at which the tomography image corresponds. The color of the cycle indicates the average thickness of the electrode. The cycling test was performed at 25 mA g^{-1} current and room temperature.

with the electrode returning to the initial state. The result is in good agreement with the findings reported previously.[19,20] The irreversibility of the PG electrode, due to the partial retention of intercalated $AlCl_4^-$,[24] leads to the irreversible thickness variation. In results reported in our previous manuscript by ex situ tomography, it is suggested that the electrode porosity changes can be one of the main reasons for the anions trapping in the PG,[24] most likely associated with the PG structure close to a single crystal, achieved by the heat decomposition of a polymeric film. The severe volumetric variation and the associated mechanical stress suggest limited electrochemical stability of the system upon long-term cycling, however, as demonstrated by our previous results,[20,23] and as well by results of several other groups,[16,18,19] the Al/graphite system can sustain a large number of cycles with only a limited capacity degradation. Nevertheless, the electrode volumetric variation is a challenge for the scaling up and the realization of large format batteries.

3. Conclusions

In conclusion, we have employed simultaneous ED-XRD and tomography to characterize the Al/graphite battery system. The obtained results show that the $AlCl_4^-$ intercalation in graphite proceeds on a multi-staging path. Based on voltage profile behavior and ED-XRD pattern evolution, it is indicated that the initial phase is a mixed-staged region, followed by a process with the characteristics of a two-staged region. Comparing NG to PG indicates limited electrochemical reversibility of the second system due to the partial retention of $AlCl_4^-$ in the graphite layer. An increase of inhomogenous strain upon cycling is observed for the PG electrode, most likely related to its poor electrochemical reversibility. Finally, the tomography results revealed an elevated volumetric change of the PG electrode upon cycling compared to the NG electrode. Moreover, the volumetric variation of the PG is irreversible in agreement

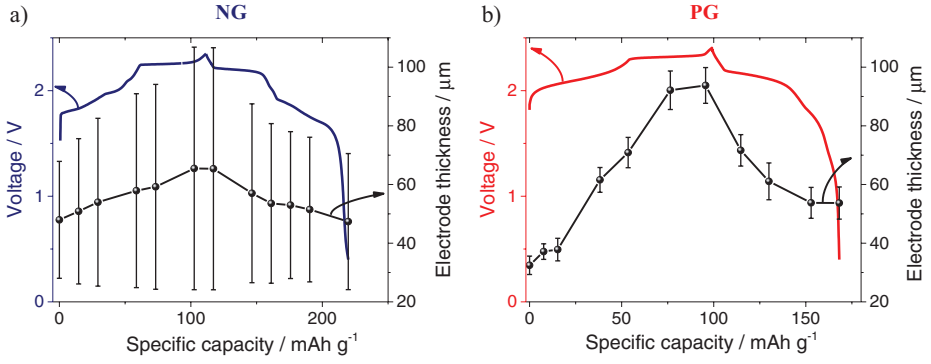

Figure 6. Electrode thickness evolution upon cycling for the a) NG electrode and b) PG electrode. The reported data are for the first cycle of the cycling test performed at 25 mA g^{-1} current and room temperature.

© 2020 The Authors. Published by Wiley-VCH GmbH

with the other reported results. The information obtained in this study gives a new understanding of the anion intercalation process of the graphite electrode. The new insight is of fundamental importance for the future development of this class of electrochemical storage systems. Additionally, the proposed experimental setup can be of interest to investigate other battery technologies, including lithium, sodium, or potassium ion, as shown recently in the literature.[31]

4. Experimental Section

Material and Electrochemical Test: The electrolyte 1-ethyl-3-methylimidazolium chloride:aluminum trichloride EMIMCl:$AlCl_3$ in a 1:1.5 mole ratio was provided by IOLITEC, the water content of the electrolyte was lower than 100 ppm. Pyrolytic graphite foil (PG) with a thickness of 25 µm and loading of 4.7 mg cm^{-2}[16,23] employed as cathode material was purchased from Panasonic. The natural graphite powder (NG) used as cathode material was provided by PLANO GmbH.[20] The NG electrode was produced by spray deposition on a Whatman GF/A glass fiber separator. A detailed description could be found in the previous work.[20,52] It has to be mentioned that the procedure used was not optimal to prepare electrodes. However, the choice was dictated by the lack of suitable polymeric binder and metallic current collector.[20,52] The NG electrodes employed in the tests had an active material loading of 3.5–5 mg cm^{-2}. In previous work, it was found that NG and PG did not present relevant structural or functional group differences.[20] A different morphology characterized the two graphite materials, with the NG composed of 200–300 µm large and 20–40 µm thick graphite flakes, and the PG constituted of highly oriented graphite films with submicron-roughness on the surface, without any particles shape.[20] The PG and NG electrodes were cut in 4 mm disks, afterward dried overnight at a temperature of 110 °C under vacuum before using them for electrochemical tests. The electrochemical measurements were performed using Teflon Swagelok type T cells.[23] Figure 1a in the Supporting Information shows a picture of the cell used for the test. The 4 mm aluminum disk, the separator (Whatman GF/A glass fiber) soaked with the electrolyte, and the cathode were placed on top of each other and pressed together by the glassy carbon current collector. The diameter of the electrodes was selected to fit into the selected field of view of the tomographic camera (4 mm × 0.5 mm). The cycling tests of Al/EMIMCl:$AlCl_3$/PG and of the Al/EMIMCl:$AlCl_3$/NG cells were carried out applying a specific current of 25 mA g^{-1} in the voltage range 0.4–2.45 V. The test cell body was made from PTFE, while 4 mm glassy carbon rods were used as current collectors. This cell configuration was selected for its stability against the highly corrosive 1-ethyl-3-methylimidazolium chloride:aluminum trichloride EMIMCl:$AlCl_3$ electrolyte.[20,23,53,54]

Beamline Setup and Operando Measurements: For probing the sample, the white beam with an energy range of 6–120 keV generated by the 7T multipole wiggler at the EDDI beamline, BESSY II, Berlin, was filtered by 5 mm of Al to suppress lower energies, which were known to be capable of influencing the sample chemistry. The transmitted part of the primary beam was detected behind the sample by the imaging system, consisting of a 200 µm thick LuAG:Ce scintillator, a Schneider Optics macro lens with a magnification factor of ≈4.4, and a PCO DIMAX high-speed camera. The camera was equipped with a CMOS chip with a pixel pitch of 11 µm, resulting in an effective pixel size of 2.5 µm that was kept out of the direct beam by using a mirror. The field of view was set to ≈4 mm × 0.5 mm (length × height). The part of the beam diffracted by the sample passed through a slit system and was detected by a Canberra GL0110 multi-channel Ge detector under a selected fix angle of $2\theta = 6°$. The battery was placed on a rotating stage while being remotely controlled using a potentiostat within the beamline hutch, and kept electrochemically cycling at 25 mA g^{-1} through the complete characterization process. Every 15 min, one synchrotron X-ray tomography and energy-dispersive diffraction measurement were taken simultaneously during the 180° rotation of the cell. Each complete measurement took around 90 s. Figure 1b in the Supporting Information shows a photographic picture of the beamline setup, while a schematic is reported in Figure 1c in the Supporting Information.[29–31]

Strain Evaluation: In order to decouple the contribution of the crystallite size and the inhomogenous strain effect on the ED-XRD peak broadening, the WH plot[55] was used in the reciprocal space for different stages. A Gaussian peak profile was assumed to obtain the WH plot in order to deconvolute the strain contribution from the size one.[55] The integrated width of the physical broadened profile B_f of the sample was consisted of the sum of the size component B_s and strain component B_d. The size component B_s did not depend on the diffraction angle. The strain component B_d increased linearly with the order of the peak. For Gaussian peak profiles, one assumed Equation (1)[56]

$$\left(B_f^*\right)^2 = \left(B_s^*\right)^2 + \left(B_d^*\right)^2 = \left(B_s^*\right)^2 + \left(2ed^*\right)^2 \tag{1}$$

$$\frac{B_d^*}{2d^*} = e = \Delta d/d \tag{2}$$

$$d^* = \frac{1}{d} = 2\frac{\sin(\theta)}{\lambda} \tag{3}$$

$$B_f^* = B_f \frac{\cos\theta}{\lambda} \tag{4}$$

$$B_s^* = \frac{1}{l} \tag{5}$$

where e is the strain variation within the domains (Equation (2)), λ is the wavelength, and by dividing the peak area by the peak intensity, one obtains B_f (integral breadth) (Equation (4)). The WH plot $(B_f^*)^2$ w as gotten over $(d^*)^2$ for all the different stages (Equation (3)). The plots were fitted by a straight line, where the slope is $(2\ e)^2$ and the intersection of the straight line represents the lateral domain size l (Equation (5)).

Tomographic Image Analysis: The resulting volumes were filtered using a 3D adaptive filter, followed by a region merging algorithm.[57] The graphite electrode was segmented by its defining gray value and manually refined by removing unrelated outlying areas. The electrode thickness was determined by a volume-based local thickness method, where each voxel was assigned the diameter of the largest sphere that contained the voxel and was located entirely within the structure.[58]

Supporting Information

Supporting Information is available from the Wiley Online Library or from the author.

Acknowledgements

The European Commission funded this research within the H2020 ALION project under contract 646286 and the German Federal Ministry of Education and Research in the AlSiBat project under contract 03SF0486 and the project ALIBATT under contract 03XP0128E. The authors thank the Helmholtz-Zentrum Berlin for the allocation of beamtime at the EDDI synchrotron beamline, Bessy II. Open access funding enabled and organized by Projekt DEAL.

Conflict of Interest

The authors declare no conflict of interest.

© 2020 The Authors. Published by Wiley-VCH GmbH

Keywords

Al batteries, graphite intercalation compounds, operando characterization, X-ray diffraction

Received: May 5, 2020
Revised: June 19, 2020
Published online: September 6, 2020

[1] G. A. Elia, K. Marquardt, K. Hoeppner, S. Fantini, R. Lin, E. Knipping, W. Peters, J.-F. Drillet, S. Passerini, R. Hahn, *Adv. Mater.* **2016**, *28*, 7564.
[2] L. Xie, K. Funatani, G. Totten, *Handbook of Metallurgical Process Design (Materials Engineering)*, Vol. 24, CRC Press, Boca Raton, FL **2004**.
[3] U.S. Geological Survey, G. S. Circular, *Mineral Commodities Summaries*, US Government Printing Office, Washington DC **2015**.
[4] M. Fleischer, Geological Survey Circular, 285, U.S. Geological Survey, US Government Printing Office, Washington DC **1953**.
[5] T. Leisegang, F. Meutzner, M. Zschornak, W. Münchgesang, R. Schmid, T. Nestler, R. A. Eremin, A. A. Kabanov, V. A. Blatov, D. C. Meyer, *Front. Chem.* **2019**, *7*, 268.
[6] S. Wang, Z. Yu, J. Tu, J. Wang, D. Tian, Y. Liu, S. Jiao, *Adv. Energy Mater.* **2016**, *6*, 1600137.
[7] S. Wang, S. Jiao, J. Wang, H.-S. Chen, D. Tian, H. Lei, D.-N. Fang, *ACS Nano* **2017**, *11*, 469.
[8] K. Suto, A. Nakata, H. Murayama, T. Hirai, J. Yamaki, Z. Ogumi, *J. Electrochem. Soc.* **2016**, *163*, A742.
[9] S. Wang, K. V. Kravchyk, S. Pigeot-Rémy, W. Tang, F. Krumeich, M. Wörle, M. I. Bodnarchuk, S. Cassaignon, O. Durupthy, S. Zhao, C. Sanchez, M. V. Kovalenko, *ACS Appl. Nano Mater.* **2019**, *2*, 6428.
[10] H. Wang, Y. Bai, S. Chen, X. Luo, C. Wu, F. Wu, J. Lu, K. Amine, *ACS Appl. Mater. Interfaces* **2015**, *7*, 80.
[11] J. Bitenc, N. Lindahl, A. Vizintin, M. E. Abdelhamid, R. Dominko, P. Johansson, *Energy Storage Mater.* **2020**, *24*, 379.
[12] T. Gao, X. Li, X. Wang, J. Hu, F. Han, X. Fan, L. Suo, A. J. Pearse, S. B. Lee, G. W. Rubloff, K. J. Gaskell, M. Noked, C. Wang, *Angew. Chem., Int. Ed.* **2016**, *55*, 9898.
[13] H. Yang, L. Yin, J. Liang, Z. Sun, Y. Wang, H. Li, K. He, L. Ma, Z. Peng, S. Qiu, C. Sun, H.-M. Cheng, F. Li, *Angew. Chem., Int. Ed.* **2018**, *57*, 1898.
[14] X. Yu, M. J. Boyer, G. S. Hwang, A. Manthiram, *Chem* **2018**, *4*, 586.
[15] W. Wang, Z. Cao, G. A. Elia, Y. Wu, W. Wahyudi, E. Abou-Hamad, A.-H. Emwas, L. Cavallo, L.-J. Li, J. Ming, *ACS Energy Lett.* **2018**, *3*, 2899.
[16] M.-C. Lin, M. Gong, B. Lu, Y. Wu, D.-Y. Wang, M. Guan, M. Angell, C. Chen, J. Yang, B.-J. Hwang, H. Dai, *Nature* **2015**, *520*, 324.
[17] S. Wang, K. V. Kravchyk, A. N. Filippin, U. Müller, A. N. Tiwari, S. Buecheler, M. I. Bodnarchuk, M. V. Kovalenko, *Adv. Sci.* **2018**, *5*, 1700712.
[18] S. Wang, K. V. Kravchyk, F. Krumeich, M. V. Kovalenko, *ACS Appl. Mater. Interfaces* **2017**, *9*, 28478.
[19] K. V. Kravchyk, S. Wang, L. Piveteau, M. V. Kovalenko, *Chem. Mater.* **2017**, *29*, 4484.
[20] G. A. Elia, N. A. Kyeremateng, K. Marquardt, R. Hahn, *Batteries Supercaps* **2018**, *2*, 83.
[21] K. V. Kravchyk, C. Seno, M. V. Kovalenko, *ACS Energy Lett.* **2020**, *5*, 545.
[22] D. Novko, Q. Zhang, P. Kaghazchi, *Phys. Rev. Appl.* **2019**, *12*, 024016.
[23] G. A. Elia, I. Hasa, G. Greco, T. Diemant, K. Marquardt, K. Hoeppner, R. J. Behm, A. Hoell, S. Passerini, R. Hahn, *J. Mater. Chem. A* **2017**, *5*, 9682.
[24] G. Greco, D. Tatchev, A. Hoell, M. Krumrey, S. Raoux, R. Hahn, G. A. Elia, *J. Mater. Chem. A* **2018**, *6*, 22673.
[25] C.-J. Pan, C. Yuan, G. Zhu, Q. Zhang, C.-J. Huang, M.-C. Lin, M. Angell, B.-J. Hwang, P. Kaghazchi, H. Dai, *Proc. Natl. Acad. Sci. U. S. A.* **2018**, *115*, 5670.
[26] W. Rüdorff, *Z. Phys. Chem.* **1940**, *42*, 121.
[27] N. Daumas, A. Herold, *C. R. Hebd. Seances Acad. Sci., Ser. C* **1969**, *268*, 373.
[28] K. V. Kravchyk, M. V. Kovalenko, *Adv. Energy Mater.* **2019**, *9*, 1901749.
[29] C. Genzel, I. A. Denks, J. Gibmeier, M. Klaus, G. Wagener, *Nucl. Instrum. Methods Phys. Res., Sect. A* **2007**, *578*, 23.
[30] F. García-Moreno, C. Jiménez, P. H. Kamm, M. Klaus, G. Wagener, J. Banhart, C. Genzel, *J. Synchrotron Radiat.* **2013**, *20*, 809.
[31] F. Sun, K. Dong, M. Osenberg, A. Hilger, S. Risse, Y. Lu, P. H. Kamm, M. Klaus, H. Markötter, F. García-Moreno, T. Arlt, I. Manke, *J. Mater. Chem. A* **2018**, *6*, 22489.
[32] G. A. Elia, J.-B. Ducros, D. Sotta, V. Delhorbe, A. Brun, K. Marquardt, R. Hahn, *ACS Appl. Mater. Interfaces* **2017**, *9*, 38381.
[33] M. S. Seehra, U. K. Geddam, D. Schwegler-Berry, A. B. Stefaniak, *Carbon* **2015**, *95*, 818.
[34] H. Shi, J. Barker, M. Y. Saïdi, R. Koksbang, L. Morris, *J. Power Sources* **1997**, *68*, 291.
[35] Y. Wu, M. Gong, M. C. Lin, C. Yuan, M. Angell, L. Huang, D. Y. Wang, X. Zhang, J. Yang, B. J. Hwang, H. Dai, *Adv. Mater.* **2016**, *28*, 9218.
[36] C. Liu, Z. Liu, H. Niu, C. Wang, Z. Wang, B. Gao, J. Liu, M. Taylor, *MethodsX* **2019**, *6*, 2374.
[37] A. Heckmann, P. Meister, L.-Y. Kuo, M. Winter, P. Kaghazchi, T. Placke, *Electrochim. Acta* **2018**, *284*, 669.
[38] G. Schmuelling, T. Placke, R. Kloepsch, O. Fromm, H.-W. Meyer, S. Passerini, M. Winter, *J. Power Sources* **2013**, *239*, 563.
[39] P. Meister, G. Schmuelling, M. Winter, T. Placke, *Electrochem. Commun.* **2016**, *71*, 52.
[40] M. Balabajew, H. Reinhardt, N. Bock, M. Duchardt, S. Kachel, N. Hampp, B. Roling, *Electrochim. Acta* **2016**, *211*, 679.
[41] C. Sole, N. E. Drewett, L. J. Hardwick, *Faraday Discuss.* **2014**, *172*, 223.
[42] R. T. Carlin, H. C. De Long, J. Fuller, P. C. Trulove, *J. Electrochem. Soc.* **1994**, *141*, L73.
[43] S. Rothermel, P. Meister, G. Schmuelling, O. Fromm, H.-W. Meyer, S. Nowak, M. Winter, T. Placke, *Energy Environ. Sci.* **2014**, *7*, 3412.
[44] B. Özmen-Monkul, M. M. Lerner, *Carbon* **2010**, *48*, 3205.
[45] J. A. Seel, J. R. Dahn, *J. Electrochem. Soc.* **2000**, *147*, 892.
[46] H. Chen, F. Guo, Y. Liu, T. Huang, B. Zheng, N. Ananth, Z. Xu, W. Gao, C. Gao, *Adv. Mater.* **2017**, *29*, 1605958.
[47] H. Stanjek, W. Häusler, *Hyperfine Interact.* **2004**, *154*, 107.
[48] J.-M. Zhang, Y. Zhang, K.-W. Xu, V. Ji, *Solid State Commun.* **2006**, *139*, 87.
[49] N. S. Ramgir, Y. K. Hwang, I. S. Mulla, J.-S. Chang, *Solid State Sci.* **2006**, *8*, 359.
[50] P. Zavalij, V. K. Pecharsky, *Fundamentals of Powder Diffraction and Structural Characterization of Materials*, Springer US, Boston, MA **2009**.
[51] C. Suryanarayana, M. G. Norton, *X-Ray Diffraction*, Springer US, Boston, MA **1998**.
[52] U. Ulissi, G. A. Elia, S. Jeong, J. Reiter, N. Tsiouvaras, S. Passerini, J. Hassoun, *Chem. - Eur. J.* **2018**, *24*, 3178.

© 2020 The Authors. Published by Wiley-VCH GmbH

[53] L. P. Davis, C. J. Dymek, J. J. P. Stewart, H. P. Clark, W. J. Lauderdale, *J. Am. Chem. Soc.* **1985**, *107*, 5041.
[54] T. Jiang, M. J. J. Chollier Brym, G. Dubé, A. Lasia, G. M. M. Brisard, *Surf. Coat. Technol.* **2006**, *201*, 1.
[55] G. Williamson, W. Hall, *Acta Metall.* **1953**, *1*, 22.
[56] X. Guo, W. Braun, B. Jenichen, V. M. Kaganer, B. P. Tinkham, A. Trampert, K. H. Ploog, *J. Appl. Phys.* **2006**, *100*, 023536.
[57] R. Nock, F. Nielsen, *IEEE Trans. Pattern Anal. Mach. Intell.* **2004**, *26*, 1452.
[58] T. Hildebrand, P. Rüegsegger, *J. Microsc.* **1997**, *185*, 67.

© 2020 The Authors. Published by Wiley-VCH GmbH